RESEARCH PAPER

Two-point statistics of coherent structures in turbulent flow over riblet-mounted surfaces

Weipeng Li[1] · Hong Liu[1]

Abstract

Direct numerical simulations (DNS) of turbulent flow over a drag-reducing and a drag-increasing riblet configuration are performed. Three-dimensional two-point statistics are presented for the first time to quantify the interaction of the riblet surfaces with the coherent, energy-bearing eddy structures in the near-wall region. Results provide statistical evidence that the averaged organization of the streamwise vortices in the drag-reducing case is lifted above the riblet tip, while in the drag-increasing case the streamwise vortices are embedded further into the riblet cove. In the spanwise direction, the cores of the streamwise vortices over the riblet surfaces are shown to be closer to each other than those for flow over the smooth wall, and wider riblet spacing leads to more reduction on their spanwise distances. In the cases with riblets the streamwise vortices have longer streamwise lengths, but their inclination angles do not change much.

Keywords Turbulent drag reduction · Riblets · Coherent structures

1 Introduction

Riblets are micro-grooved structures that are aligned parallel to the mean streamwise direction of the fluid flow. They are inspired by the skin of fast-swimming sharks and have been proved to passively reduce the turbulence skin friction up to 8%, despite an increase in the wetted surface area. Turbulent drag reduction with riblets has been an active subject of scientific research for the last three decades. Over the years, excellent surveys and reviews have been conducted, covering aspects of drag reduction performance and optimization, mechanism of operation, applications of riblet-mounted surfaces, and fabricating and manufacture of the riblet-mounted surfaces [1–5]. However, the operation mechanisms of the riblets have not been clearly resolved, especially with respect to their interaction with the coherent, energy-bearing eddy structures in the near-wall region.

✉ Weipeng Li
liweipeng@sjtu.edu.cn

1 School of Aeronautics and Astronautics, Shanghai Jiao Tong University, Shanghai 200240, China

The study by Bacher and Smith [6] analyzed the dye and hydrogen bubble visualizations for a turbulent flow over riblets and attempted to determine the changes in turbulent structures. They reported that the generation of the cross-stream secondary vortices inside the riblet valley is able to weaken the momentum exchange properties and to inhibit the spanwise concentration of the low-speed fluid into streak formation. With the aid of a three-dimensional particle tracking velocimetry, Suzuki and Kasagi [7] measured the statistics of all three velocity components of a turbulent flow over riblets. They argued that the mechanism proposed by Bacher and Smith [6] was not convincing. On the contrary, the generation of the cross-stream secondary vortices should enhance the turbulent momentum transport and deteriorate the drag reduction effect of the riblets. They proposed that the drag reduction mechanism is closely related with the suppression of near-wall vortex generation and/or the damping of the vortices by the attenuation of the turbulent kinetic energy redistribution from the streamwise component to the spanwise one in the region above the riblet valley.

Under Stokes flow conditions, theoretical investigations of the viscous sublayer on surfaces with riblets have been conducted. To this end, Bechert and Bartenwerfer [8] hypothesized that the riblets do impede the instantaneous crossflow in the viscous sublayer, resulting in a reduction of the tur-

bulent momentum exchange and consequently a shear stress reduction. Furthermore, Luchini et al. [9] proposed a quantitative characterization of the differential effect of the wall on parallel flow and cross-flow in terms of the difference of two protrusion heights.

The work of Tardu [10] analyzed the effect of the riblets on drag producing vortical structures by means of near wall vorticity dynamics. It was conjectured that the riblets shorten the time period necessary for the spatiotemporal development of the low speed streak instability in drag reducing configurations. The break-up of the spanwise vortex filaments is inhibited, and only those spanwise vortical structures with low Reynolds numbers are subjected to long-wavelength instability resulting in small growth rates. An extensive analysis combined with some observations inferred from direct numerical simulations (DNS) suggested a chain of events, which leads to a secondary x-dependent wall normal vorticity.

A study by Choi et al. [11] performed DNS of turbulent channel flow with only the lower wall mounted with riblets. With examinations of the instantaneous flow fields, they proposed a drag reduction mechanism: drag-reducing riblets are able to restrict the location of the streamwise vortices above the wetted surface, such that only a limited area of the riblets is exposed to the downwash of high-speed fluid that the streamwise vortices induce, whereas for the drag increase riblets the streamwise vortices are sometimes submerged into the riblet valley, which bring about high wall shear regions inside the valley. This mechanism was supported by the experimental study of Lee and Lee [12]. A difference observed in the experimental visualizations was that for the drag increase condition, most parts of the streamwise vortices are immersed into the valleys of the riblets. Recent numerical study by Martin and Bhushan [13] supported this mechanism that lift-up of the streamwise vortices by the riblet peaks, and they gave a riblet design principle to get an optimal drag reduction performance.

The study done by García-Mayoral and Jiménez [14] focused on the breakdown of the viscous regime as the riblets get larger than the viscous limit and tried to determine the parameters that best describe the extent of the linear region and the mechanism that controls the breakdown. Their analysis suggested that the localization of the streamwise vortices, which appears above the riblets, but not to lodge within the riblets, is not related to the drag reduction mechanism, which is contrary to previous studies in Refs. [11–13]. They argued that the appearance of essentially two-dimensional spanwise rollers (induced by Kelvin–Helmholtz instability) is the main change to characterized the breakdown and accounts for the drag degradation observed past the breakdown of the viscous regime.

As discussed above, the most important clue to reveal the drag reduction mechanism is to quantify the interaction of the riblet surface with the near-wall turbulence coherent structures. However, in the aforementioned studies identifications of the near-wall turbulence coherent structures were mostly obtained from the snapshots of instantaneous flow-fields [6,11,12] or theoretical estimations [8–10,14,15]. Quantitative and statistical analyses are required. In the present study, by means of three-dimensional spatial correlations, we are going to analyze the effects of riblets on the near-wall coherent structures with DNS data of turbulent flow over a drag-reducing and a drag-increasing riblet configuration. The work is organized as follows. Section 2 describes the numerical algorithm for the DNS setting. Validations of the DNS data are given in Sect. 2. Detailed analyses of the coherent structures are discussed in Sect. 3. Finally, concluding remarks are presented in Sect. 6.

2 Numerical algorithm

2.1 Numerical methods

The governing equations are three-dimensional unsteady compressible Navier-Stokes equations. A finite difference approach is used to solve the governing equations. The computational fluid dynamics (CFD) solver has been extensively validated in previous works both for wall-bounded turbulent flows and free jets [16–19]. In order to meet low-dispersive and low-dissipative requirements of turbulent flows, the convective terms are discretized by means of a six-order compact differencing scheme in transformed curvilinear coordinates [20,21]. An eighth-order low-pass spatial filtering scheme (with optimization parameter $\alpha_f = 0.493$) [20] is applied at each time step on the conservative variables to ensure numerical stability. Viscous terms are evaluated by a sixth-order central differencing scheme. Alternate directional implicit symmetric Gauss–Seidel (ADI-SGS) scheme [22] is performed for the time integration. A second-order temporal accuracy is obtained with three local sub-iterations to converge the Newton–Raphson sub-iterative process. The time step Δt is equal to $0.001\delta_{in}/a_\infty$, where δ_{in} denotes the inlet boundary-layer velocity thickness and a_∞ is the freestream sound speed. The time step is selected to ensure the Courant–Friedrichs–Lewy number is less than unity. With respect to the viscous units, the viscous time step $\Delta t^+ = \Delta t u_\tau^2/\upsilon$ is less than 0.004, where u_τ denotes friction velocity on the smooth wall and υ denotes kinematic viscosity.

2.2 Inflow conditions

The freestream Mach number M is set as 0.3. The flow is in a low Mach number and belongs to incompressible regime [23]. The Reynolds number based on the freestream

streamwise velocity U_∞ and inlet velocity boundary-layer thickness δ_{in} is $Re_{\delta_{in}} = 1.1 \times 10^4$. The Reynolds number based on the momentum boundary-layer thickness is $Re_\theta = 1300$, and the Reynolds number based on the friction velocity is $Re_\tau = 350$. Generation of a spatially developing turbulent inflow without a simulation of the laminar-to-turbulent transition process is one of the most important techniques in large-eddy simulations and DNS. In the present work, prior to the study of the drag reduction, a simulation of zero-pressure-gradient flat plate is performed to generate a spatially developing turbulent inflow with a recycling and rescaling technique. The flow field is decomposed into a time-averaged and fluctuating part, and the flow properties at a downstream station are recycled and reintroduced as the inflow boundary condition according to an appropriate scaling law [24]. To avoid numerical "drift" phenomena (as discussed in Ref. [25]), the mean flow fields at the inflow are kept constant, and only density and velocity fluctuations are recycled and rescaled to the inflow. The mean flow field at the inflow is obtained from a two-dimensional Reynolds averaged Navier–Stokes (RANS) simulation of a flat plate with Spalart–Allmaras turbulence model [26]. A weighted function, which was proposed by Lund et al. [27], is used to combine the inner- and outer-layer fluctuations. A dynamic reflection operation proposed by Morgan et al. [28] is applied to eliminate spurious spatial correlations at downstream stations and reduce unphysical temporal correlations related to the recycling procedure. To yield faster transition to turbulent state, the enforcement of initial velocity fields is similar to the approach developed by Sandham et al. [29] and Pirozzoli et al. [24]. Starting from the initial condition, the governing equations are integrated forward in time until the numerical solutions reaches statistically steady states. Then flow properties at the recycling position are stored and reintroduced at the inlet in the simulation of the cases with riblets. The total collection time is about $90\delta_{in}/U_\infty$. With this time duration, validations of the turbulent inflow are carried out to examine the time-averaged and statistical quantities.

2.3 Computational domain and grid spacing

The kernel computational domain for the generation of turbulent inflow has an overall size of $L_x \times L_y \times L_z = 12\delta_{in} \times 2\delta_{in} \times 1.168\delta_{in}$, where x, y and z stand, respectively, for the streamwise, wall-normal and spanwise directions. The computational domain is discretized by a mesh consisting of $N_x \times N_y \times N_z = 456 \times 130 \times 488$ grid points that are uniformly distributed in the streamwise and spanwise directions. The mesh is stretched in the wall-normal direction (with $N_\delta = 105$ grid points inside one boundary-layer thickness) according to smooth stretching ratios. In terms of wall units, the grid spacing in the wall normal direction varies from $\Delta y^+ = 0.85$ at the wall to $\Delta y^+ = 10$ at the boundary-layer edge.
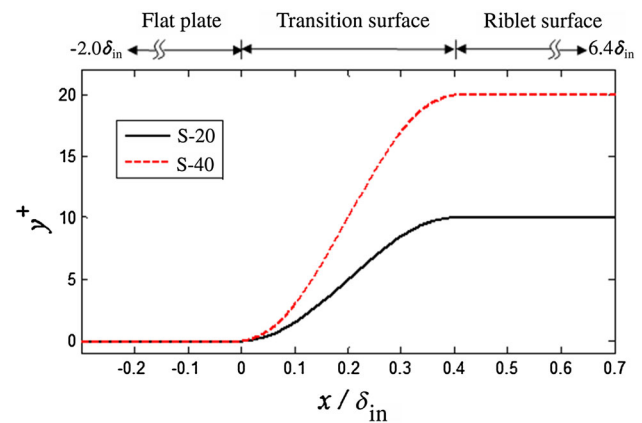

Fig. 1 Coordinates of the riblet tips

The streamwise and spanwise grid spacing are $\Delta x^+ = 10$ and $\Delta z^+ = 1$, respectively.

An additional buffer region is placed at the outlet and upper boundaries to remove turbulent fluctuations and any reflections from the boundaries. It has a length of $12\delta_{in}$ and $25\delta_{in}$ discretized by 50 and 40 grid points in the streamwise and wall-normal directions, respectively. The total grid points for the calculation of the turbulent inflow ($N_x \times N_y \times N_z = 505 \times 169 \times 488$) are 41.6 million.

Three simulation cases (termed as Baseline, S-20, and S-40) are conducted to assess the drag reduction with riblets. The Baseline case represents the basic turbulent boundary layer over a flat plate. The S-20 and S-40 cases are plates covered with riblets. Triangular riblets with ridge angle of 45° are adopted in this study. The spacing of the riblets in the S-20 and S-40 cases are $s^+ = 20$ and $s^+ = 40$, respectively. The ratios between riblet heights and the inlet momentum boundary-layer thickness are about 0.2 and 0.4 for the S-20 and S-40 case, respectively. A transition surface is set to switch the upstream flat plate to riblet surfaces. The coordinates of riblet tips are plotted in Fig. 1. The transition surface has a streamwise distance of $0.4\delta_{in}$, starting from $x = 0.0$ and ending at $x = 0.4\delta_{in}$. It has an upstream extension of $2\delta_{in}$ with smooth walls and a downstream extension of $6\delta_{in}$ with riblet configurations.

Computational grids above the riblets at a cross-flow plane are shown in Fig. 2. The grids are clustered in the vicinity of the riblet tips due to rapid variation of skin friction near the riblet tips. For each riblet, it has 21 and 41 spanwise grid points for the S-20 and S-40 cases, respectively. Similar to the simulation of the turbulent inflow, 488 grid points are used in the spanwise direction to solve 24 riblets in the S-20 case and 12 riblets in the S-40 case. In the streamwise and wall-normal directions, 325 and 130 grid points are used, respectively. An additional buffer region is placed at the outlet and upper boundaries to remove turbulent fluctuations and any reflections from the boundaries. The total grid points for the three cases ($N_x \times N_y \times N_z = 364 \times 169 \times 488$) are 30.0 million.
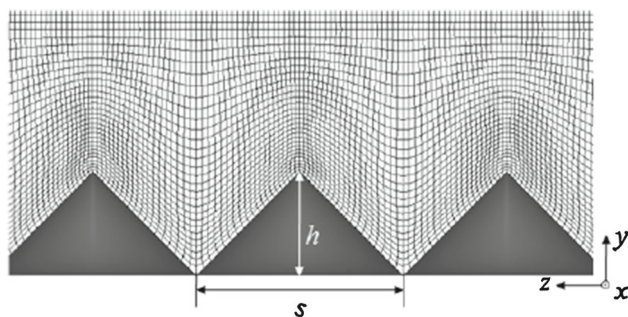
Fig. 2 Computational grids above the riblets at a cross-flow plane

2.4 Boundary conditions

No-slip adiabatic wall boundary condition is imposed at solid walls. Zero-gradient pressure condition is employed at the outlet and upper boundaries. The inlet boundary is of a turbulent boundary layer developed on a flat plate, generated using the recycling and recalling technique discussed above. For the cases of Baseline, S-20, and S-40, the simulations are initialized with a mean turbulent streamwise velocity profile, followed the (1/7)th power law. Then the stored turbulent inflow data are imposed at the inflow boundary under the forward time integration.

2.5 Validations

To assess the validity of the turbulent inflow, profiles of the time-averaged and statistics, which are averaged in the homogeneous spanwise direction, are discussed as below. Figure 3 shows the time-averaged streamwise velocity profile in a semi-logarithmic plot at the station of the inlet boundary. Theory predicts a linear scaling in the viscous sublayer with $U^+ = y^+$ and a logarithmic scaling in the overlap region with $U^+ = 2.4\lg(y^+) + 5.2$. The present DNS data agree well with the theory both in the viscous sublayer and the overlap region. Figure 4 shows the distribution of root-mean-square velocity fluctuations and Reynolds shear stress in inner scaling and outer scaling. The present results ($M = 0.3$, $Re_\theta = 1300$) show that the resolved turbulence intensities and the Reynolds shear stress are in good agreement with the incompressible DNS data at $Re_\theta = 1410$ [30], supersonic DNS data at $M = 1.4$, $Re_\theta = 1215$ [31], and compressible subsonic DNS data at $M = 0.3$, $Re_\theta = 1010$ [23]. Distribution of root-mean-square vorticity fluctuations in wall units is plotted in Fig. 5. The spanwise vorticity fluctuations for $y^+ < 25$ are significantly larger than either the streamwise or the wall-normal fluctuations, and nearly isotropic of the vorticity fluctuations are presented for $y^+ > 35$. This feature is consistent with the DNS data of Pirozzoli et al. [24], but a little bit different from the study of Álamo and Jiménez [32].
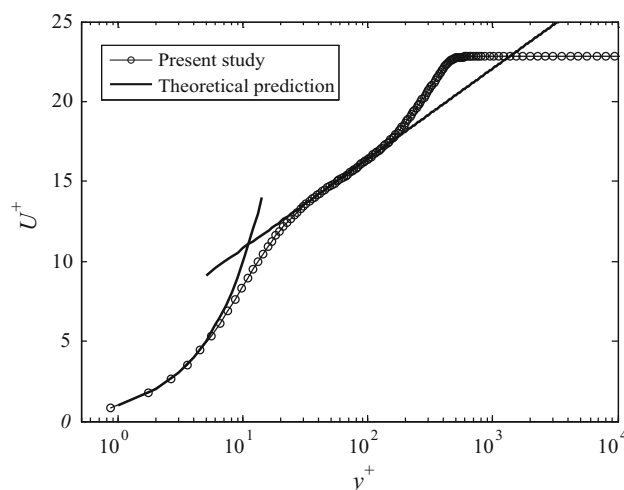

Fig. 3 Profile of the time-averaged streamwise velocity at the station of the inlet boundary

A frequency spectrum of wall pressure signals extracted at the center of inlet boundary is displayed in Fig. 6. A Hamming window function is imposed in the Fourier transform. The frequency resolution is equal to $0.0203U_\infty/\delta_{\text{in}}$. The spectrum is normalized by U_∞, δ_{in}, and the freestream dynamic pressure ($q_\infty = \rho_\infty U_\infty^2$). In the low-frequency region, the spectrum obeys a power-law scaling of $\omega^{0.3}$. In the high-frequency range, the spectrum exhibits regions with -3 and then -5 slopes. The scaling of the spectrum is similar to the observation in Ref. [33].

To assess the adequacy of the domain size in the spanwise direction, the spanwise two-point correlations for the spanwise velocity fluctuations, R_{ww}, have been computed and plotted in Fig. 7. The computational domain should be large enough in the spanwise direction so that the turbulent fluctuations are uncorrelated within one half of the periodic length of the domain. The two-point correlations at the two wall-normal locations, $y^+ = 100$ and $y^+ = 300$, approach zero, indicating that the spanwise length of the computational domain is sufficiently large.

3 Drag measurement

The instantaneous skin-friction drag is calculate by

$$D(t) = \int_A \mu_w(t) \frac{\partial u(t)}{\partial n} \mathrm{d}A, \tag{1}$$

where A denotes the wetted area of a wall surface, $\mu_w(t)$ is the temporal dynamic viscosity on the wall, and n is the coordinate normal to the surface. We define the instantaneous skin-friction coefficient as
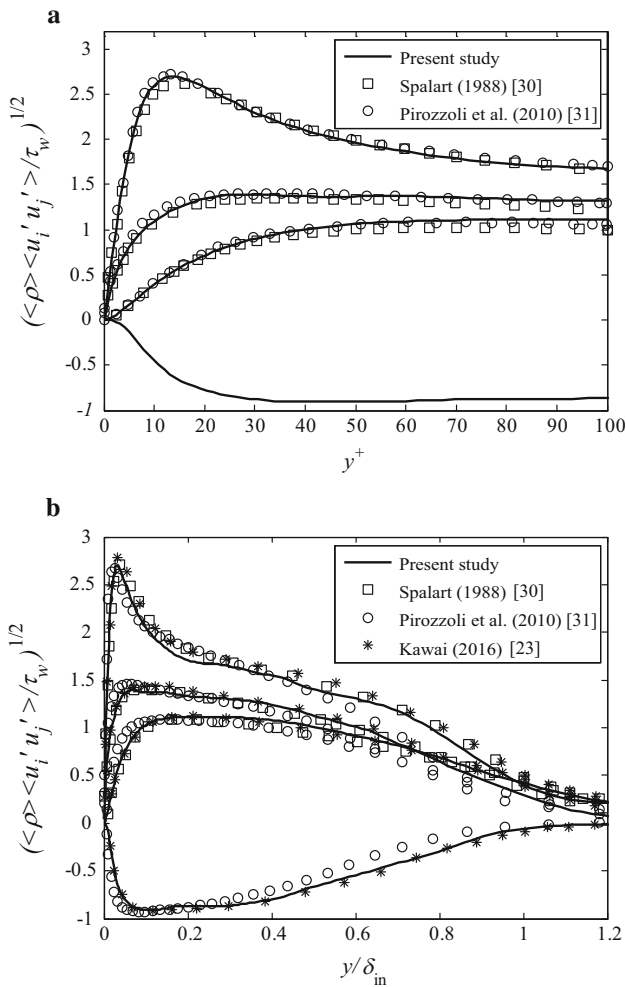
a

b

Fig. 4 Root-mean-square velocity fluctuations and Reynolds shear stress in **a** inner scaling and **b** outer scaling. Lines refer to the present DNS data: upper line, streamwise component ($i = j = 1$); mid-upper line, spanwise component ($i = j = 3$); mid-lower line, wall-normal component ($i = j = 2$); lower line, Reynolds shear stress ($i = 1$, $j = 2$). Symbols: squares represent results by Spalart [30]; circles represent results by Pirozzoli et al. [31]; stars represent results by Kawai [23]

$$C_f^*(t) = \frac{D(t)}{A_f \cdot \frac{1}{2}\rho_\infty U_\infty^2}, \qquad (2)$$

where A_f is the wetted area of the corresponding flat plate. The temporal evolutions of $C_f^*(t)$ at a station of $x = 5\delta_{in}$ and a surface within $4\delta_{in} \leqslant x \leqslant 6\delta_{in}$ are plotted in Fig. 8a, b, respectively. Stochastic and intermittent feature of the instantaneous skin-friction coefficients is depicted in Fig. 8a. With respect to the flat plate, drag reduction in the S-20 case and drag increase in the S-40 case are clearly evident in Fig. 8b. The vertical dotted lines in Fig. 8b indicate the initial and the final time for the averaging of the skin-friction coefficients. The time-averaged skin-friction coefficient is denoted as $\langle C_f^* \rangle$. Consequently, the proportion of the drag reduction or increase with the riblet surfaces are calculated by
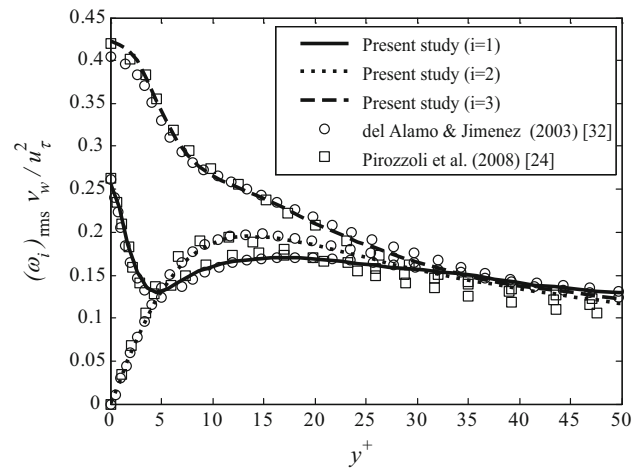

Fig. 5 Distribution of root-mean-square vorticity fluctuations in wall units. Lines refer to the present DNS data: solid line, streamwise component ($i = 1$); dotted line, wall-normal component ($i = 2$); dashed line, spanwise component ($i = 3$). Symbols: squares represent results by Pirozzoli et al. [24]; circles represent results by Álamo and Jiménez [32]
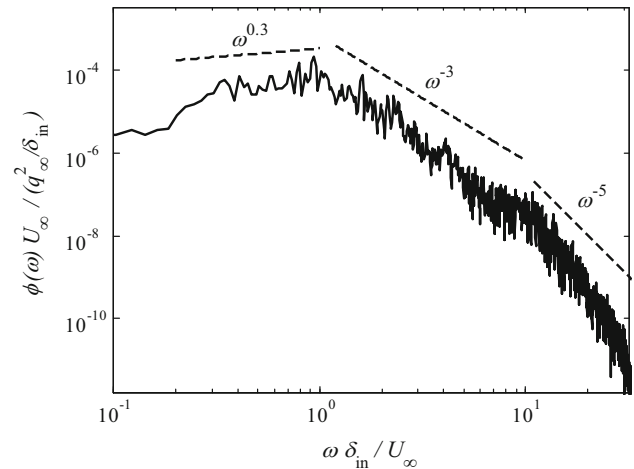

Fig. 6 Frequency spectrum of the wall pressure fluctuations extracted at the center of inlet boundary
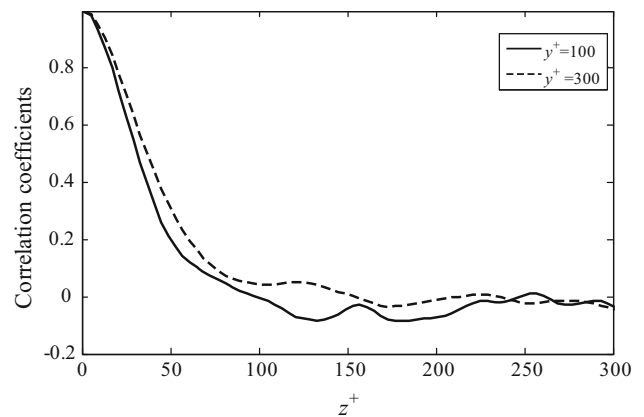

Fig. 7 Spanwise two-point correlations of the spanwise velocity fluctuations, R_{ww}, at two wall-normal locations ($y^+ = 100$ and $y^+ = 300$)
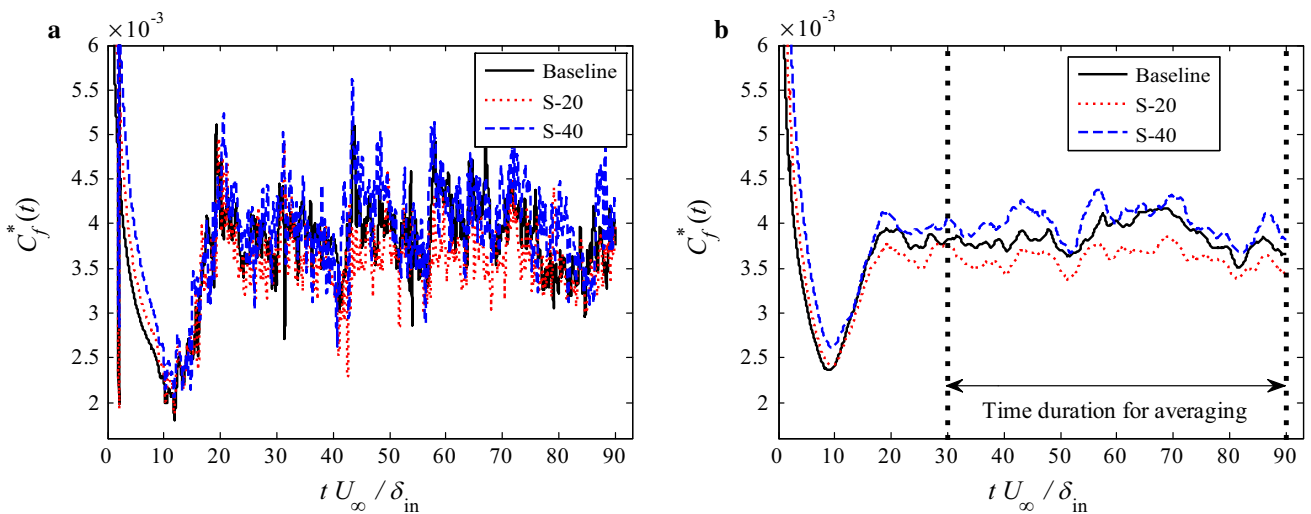
Fig. 8 Temporal evolution of instantaneous skin-friction coefficients $C_f^*(t)$ **a** a station of $x = 6\delta_{in}$ and **b** on a surface with $4\delta_{in} \leqslant x \leqslant 6\delta_{in}$. The vertical lines indicate the initial and final time for the averaging of the skin-friction coefficients

Table 1 Drag measurement using time-averaged skin-friction coefficients on a surface within $4\delta_{in} \leqslant x \leqslant 6\delta_{in}$

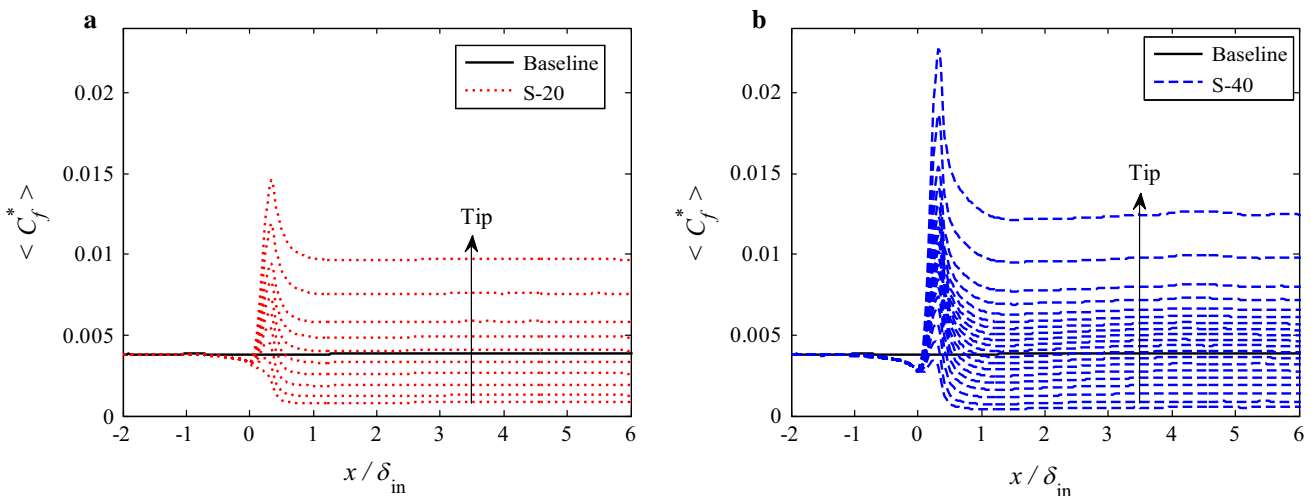| Case	DR				
	Present study (%)	Walsh [34] (%)	Bechert et al. [35] (%)	Choi et al. [11] (%)	Duan and Choudhari [36] (%)
S-20	-6.3	-2	-3.25	-5	-7.0
S-40	$+4.1$	$+3$	NA	$+2$	$+4.4$

Fig. 9 Time-averaged skin-friction coefficients at different spanwise locations of the riblets, plotted as a function of the streamwise coordinates

$$DR = \frac{\left\langle C_f^* \right\rangle_{\text{riblet}} - \left\langle C_f^* \right\rangle_{\text{smooth}}}{\left\langle C_f^* \right\rangle_{\text{smooth}}}, \qquad (3)$$

and reported in Table 1 using the surface within $4\delta_{in} \leqslant x \leqslant 6\delta_{in}$. Drag is reduced by 6.3% for the S-20 case and increased by 4.1% for the S-40 case. Experimental results of Walsh [34] and Bechert et al. [35], and DNS results of Choi et al. [11]

and Duan and Choudhari [36] with similar riblet geometries are also given in Table 1. Based on this comparison, it illustrates that the drag measurement in the present study has a qualitatively acceptable agreement with those reported in the previous studies.

Figure 9 shows the time-averaged skin-friction coefficients $\left\langle C_f^* \right\rangle$, also averaged in the spanwise direction, as a function of the streamwise coordinates. In the upstream of
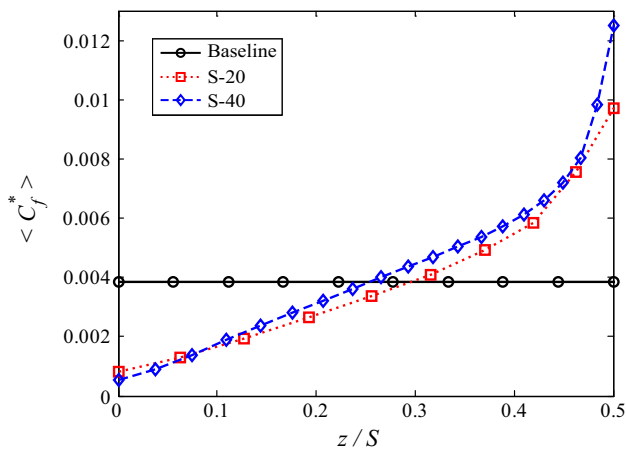
Fig. 10 Time-averaged skin-friction coefficients at different spanwise locations of the riblets ($x = 5\delta_{in}$)

the transition surface ($-2\delta_{in} \leqslant x \leqslant 0.0$), the skin-friction coefficients on the smooth-wall regions are almost identical for the three cases simulated. After a slight drop ahead of the transition surface, the skin-friction coefficients at most of the spanwise locations of the riblets increase rapidly toward peaks at $x \approx 0.3\delta_{in}$ (still within the transition surface), and then decrease to visually constant values in the downstream. The variations of the time-averaged skin-friction coefficients near the transition surface suggest that the transition surface acts as a "convergent nozzle", which accelerates the near-wall subsonic fluids and results in strong shear stresses on the wall surfaces. It implies that the protrusion of the transition surface is unable to reduce the skin-friction drag, but induces extra form drag, which agrees with the DNS study by Boomsma and Sotiropoulos [37] on three-dimensionality of the sharkskin denticle geometry. In the present study, the transition area takes approximately $1.5\delta_{in}$ in the S-20 case and $3\delta_{in}$ in the S-40 case to reach 99% of the time-averaged skin friction measured downstream of the transition area. The largest time-averaged skin-friction coefficient is obtained at the riblet tip, and the smallest value at the valley.

At a cross-flow plane where $x = 5\delta_{in}$, the time-averaged skin-friction coefficients are plotted in Fig. 10 as a function of spanwise coordinates normalized by riblet spacing (S). The coefficients near the riblet valley ($z/S = 0$) in the S-40 case are smaller than those in the S-20 case, whereas at the rest of the spanwise locations the coefficients in the S-40 case are larger than those in the S-20 case (especially near the riblet tip). Spanwise integration of the time-averaged skin-friction coefficients determines whether a total drag reduction or increase is achieved with the riblets of a given spacing. With respect to the Baseline case, local drag reductions are observed near the riblet valley, while local drag increases are observed near the riblet tip. It implies that once the drag reductions near the riblet valley are sufficient to overcome the

drag increases near the riblet tip, net drag will be reduced; otherwise increased.

4 Instantaneous and mean flow fields

Snapshots of the instantaneous streamwise vorticity and absolute vorticity from the inlet to outlet have been converted to movies, which are available to be downloaded from the website. The supplementary movies suggest that the vortical structures behave similarity except in the near-wall region for all cases simulated. Contours of instantaneous streamwise vorticity and absolute vorticity at a cross-flow plane where $x = 5\delta_{in}$ are plotted in Fig. 11 at the same time and under exactly the same inflow conditions. Major differences are limited within the inner layer of the boundary layer for $y < 0.2\delta_{in}$. The vortical structures in the near-wall region are significantly affected by the riblets. The well-known low-speed streaky structures are evident in the near-wall region of the smooth wall, for instance those marked with dashed ellipses. In the cases with riblets the low-speed streaky structures are disturbed by the riblet tips, resulting in discontinuous distributions in the spanwise direction and high values of vorticity near the tips. Quasi-streamwise vortices, which are closely associated with both ejection and sweep events and have major contributors to the Reynolds shear stress, are visualized in this cross-flow plane. In the riblet configurations, regardless of drag reduction or increase, most of the large-scale longitudinal streamwise vortices stay above the riblet tips, and flow inside the riblet coves is sufficiently calm. Note that for the drag-increasing case with wider riblet spacing, only a few strong streamwise vortices lodge inside the riblet coves, which is different with experimental visualization by Lee and Lee [12] that most streamwise vortices stay inside the riblet coves and interact actively with the increased wetted surface area. From the time-depended visualizations, it is difficult to determine the height, width and vortex centre of the quasi-streamwise vortices, although we tried the same method used by Martin and Bhushan [13]. In Sect. 5, characterization of the coherent vortical structures will be analyzed by means of two-point statistics.

The mean flow fields at a referenced y–z plane where $x = 5\delta_{in}$ are used to discuss the effects caused by the riblets. The flow properties are normalized by the freestream velocity U_{∞} and the velocity boundary-layer thickness δ_{ref} at the referenced plane ($x = 5\delta_{in}$) of the Baseline case, otherwise mentioned. Contours of the mean velocities over the riblet surfaces are displayed in Fig. 12. The mean streamwise velocities seem to be arched by the protrusion of the riblet surfaces. Lower values are presented inside the riblet coves. Steeper streamwise velocity gradients in the wall-normal direction are seen near the riblet tip, which is clearly examined from the one-dimensional view of the streamwise
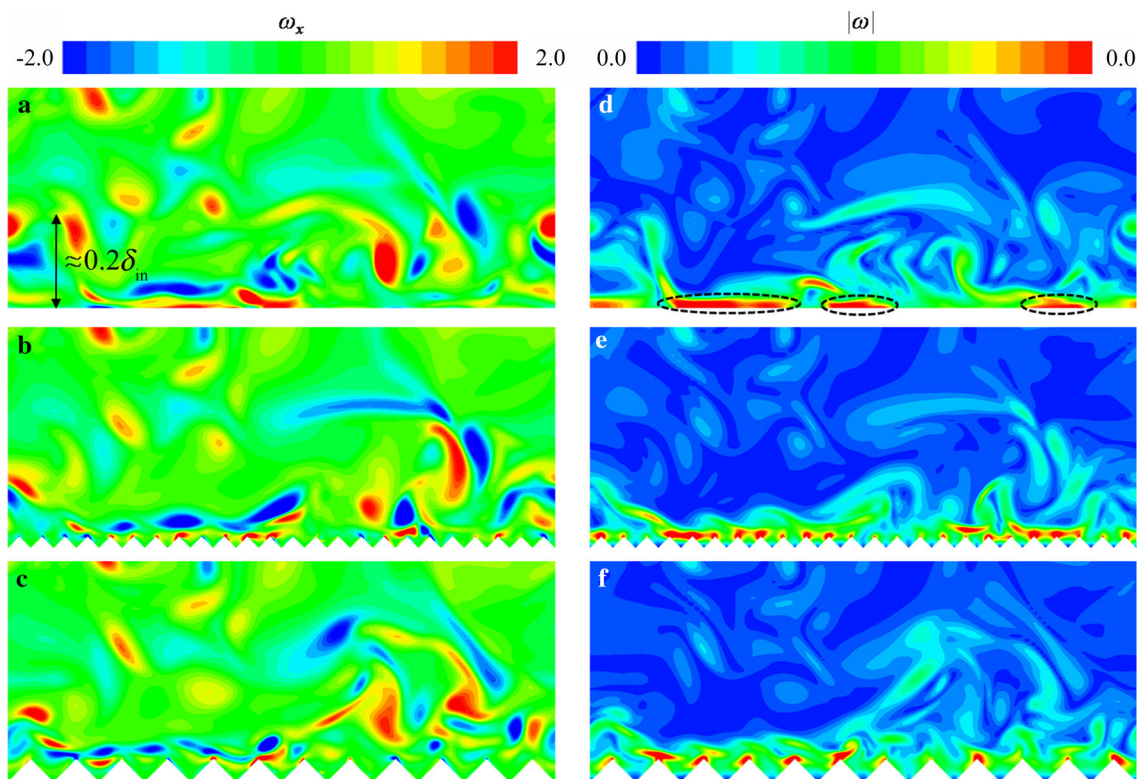
Fig. 11 Contours of instantaneous **a**–**c** streamwise vorticity and **d**–**f** absolute vorticity at a cross-flow plane where $x = 5\delta_{in}$. The plane is located at the streamwise mid of the transition surface. **a**, **d** Baseline; **b**, **e** S-20; **c**, **f** S-40

velocity at different spanwise locations, as plotted in Fig. 13. In this figure the profiles of the mean velocities are obtained by using interpolations of the velocity values in Fig. 12a, d from the calculation mesh to a vertically straight mesh, in which $y = 0$ corresponds to the valleys of the riblets. Compared to the Baseline case, no apparent difference of the mean streamwise velocity is found above $y/\delta_{ref} \approx 0.13$ for the S-20 case or above $y/\delta_{ref} \approx 0.22$ for the S-40 case. At a given y within the bounds of $y/\delta_{ref} \approx 0.13$ or 0.22, the streamwise velocities over the riblets are reduced in the riblet configurations, and wider riblet spacing results in smaller values at constant spanwise locations. Figure 12b, e displays contours of wall-normal velocity. The maximum value of the wall-normal velocity is observed above the riblet tip, with $\langle v \rangle^{max} \approx 0.003$ and 0.007 for the S-20 and S-40 case, respectively. They are one order of magnitude larger than that observed in the Baseline case ($\langle v \rangle^{max}$ smaller than 4×10^{-4} within $x < 0.2\delta_{ref}$). The minimum value is observed above the riblet valley at almost the same wall-normal location of the maximum one. If the extremes of the streamwise velocity are normalized by local mean streamwise velocities, it has $0.018/-0.008$ and $0.023/-0.012$, respectively, for the S-20 and S-40 case. The distribution of the spanwise velocity in Fig. 12c, f seems like "butterfly wings". The maximum and minimum value are presented on the sides of and beneath the

riblet tip, with $\langle w \rangle^{max,min} \approx \pm 0.002$ and ± 0.005 for the S-20 and S-40 case, respectively.

Figure 12 suggests that the riblets induce a mean secondary flow motion in the cross-flow planes. The mean secondary flow motion convects high momentum in the upper-wall region downward to the riblet valley and then brings low momentum near the riblet valley upward to the central region above the riblet tip. Wider riblet spacing results in a stronger mean secondary flow motion. The magnitude of the secondary velocity vector, $\sqrt{\langle v \rangle^2 + \langle w \rangle^2}$, is calculated. About 0.3% and 0.7% of the freestream velocity are observed respectively in the S-20 and S-40 case, which agree with the DNS data given by Choi et al. [11]. If normalized by the local mean streamwise velocity, the magnitude is about 5.3% for the S-20 case and 8.3% for the S-40 case. It indicates that the secondary flow over riblets is sufficiently strong to transport momentum in the near-wall region. In a laminar flow over riblets, since the no cross-flow motion exists, the secondary flow motion induced by the riblets is not detected [38]. For turbulent flow over riblets, the secondary flow motion is passively generated owning to the streamwise-parallel setting of the riblets and the inherent cross-flow motions of a turbulent boundary layer. It has to note that the generation of the cross-stream secondary flow motion does perhaps not explain the net drag reduction [7].
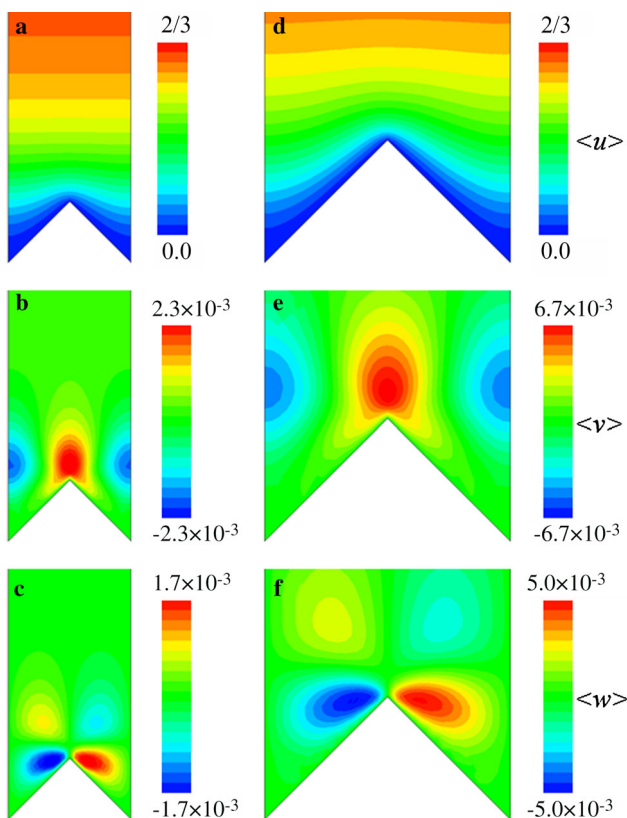
Fig. 12 Mean velocities over the riblet surfaces. **a**–**c** S-20; **d**–**f** S-40. **a**, **d** Show contours of mean streamwise velocity, **b**, **e** show contours of mean wall-normal velocity, and **c**, **f** show contours of mean spanwise velocity

Fig. 13 Profile of the mean streamwise velocity in the wall-normal direction at different spanwise locations

Fig. 14 Contours of streamwise (**a**, **d**), wall-normal (**b**, **e**), and spanwise (**c**, **f**) vorticity over the riblet surfaces. **a**–**c** S-20 case; **d**–**f** S-40 case

Figure 14 shows contours of mean streamwise, wall-normal, and spanwise vorticity. Similar features are exhibited in the riblet configurations. A mean counter-rotating streamwise vortex is presented near the riblet tip. The diameter of the vortex is approximately equal to half of the riblet width. This observation has also been reported by Choi et al. [11], El-samni et al. [39], and Boomsma and Sotiropoulos [40]. The mean streamwise vorticity at the vortex cores are $\pm 0.7\delta_{ref}/U_{\infty}$ for the S-20 case and $\pm 0.92\delta_{ref}/U_{\infty}$ for the S-40 case. These values are stronger than those observed by Choi et al. [11]. Regions of high values of the mean streamwise, wall-normal, and spanwise vorticity are presented very close to the riblet tips, indicating that the mean shear stresses are strong at these regions.

5 Near-wall coherent structures

It is well known that quasi-periodic repeating patterns of coherent structures play an important role in the dynamic behaviors of a self-sustained turbulent boundary layer. The definition of an "coherent structure" follows Robinson's concept [41]: "a three-dimensional region of the flow over which
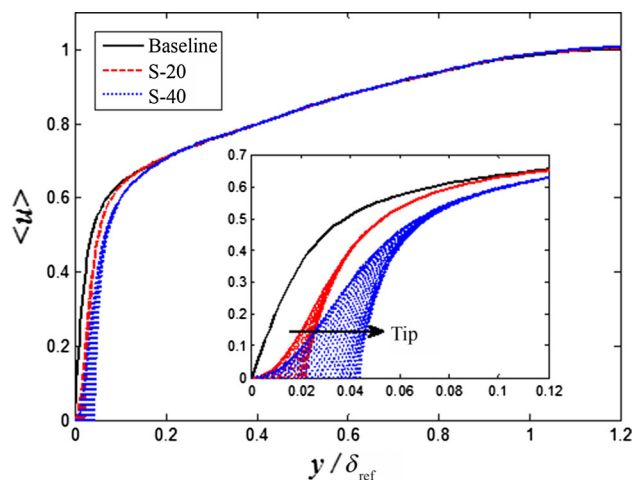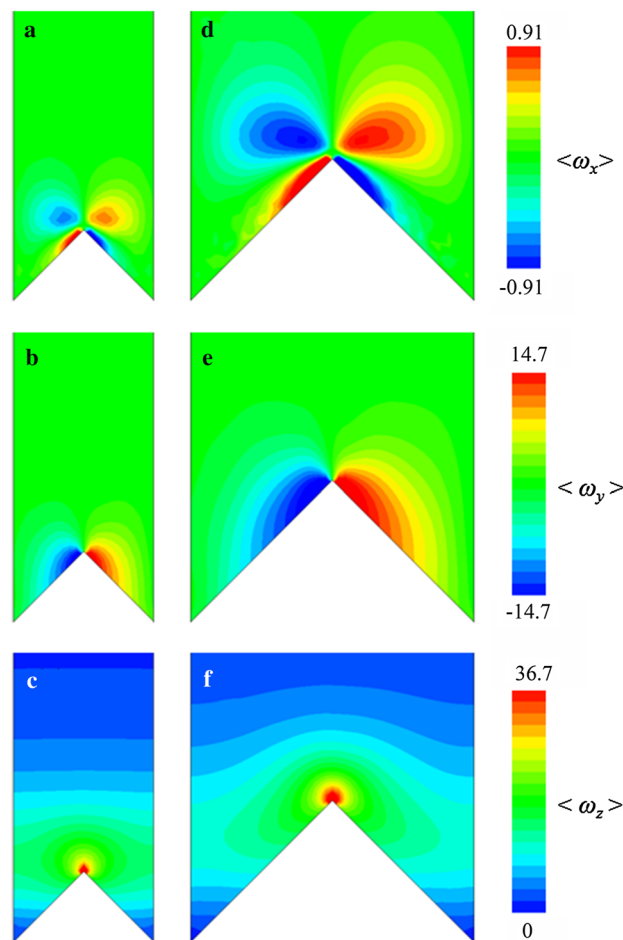
at least one fundamental flow variable exhibits significant correlation with itself or with another variable over a range of space and/or time that is significantly larger than the small-
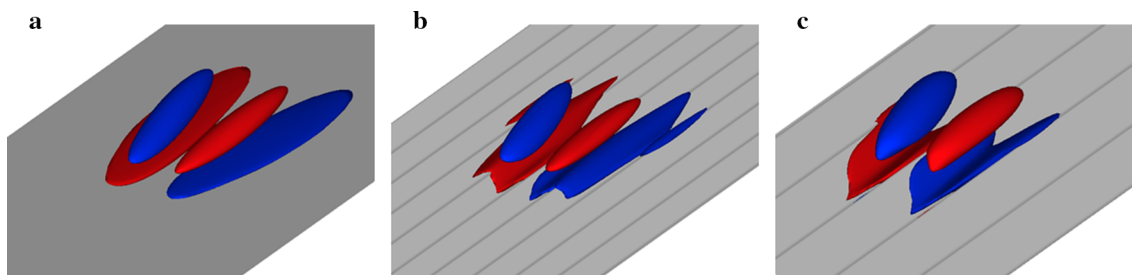
Fig. 15 Isosurfaces of the two-point cross-correlation coefficients $R(u, \omega_x)$. The red surface is defined by a positive threshold of $R(u, \omega_x) = 0.2$, and the blue surface is defined by a negative threshold of $R(u, \omega_x) = -0.2$. In the riblet configurations, the reference point locates above the riblet tip with $y \to 0$. **a** Baseline. **b** S-20. **c** S-40
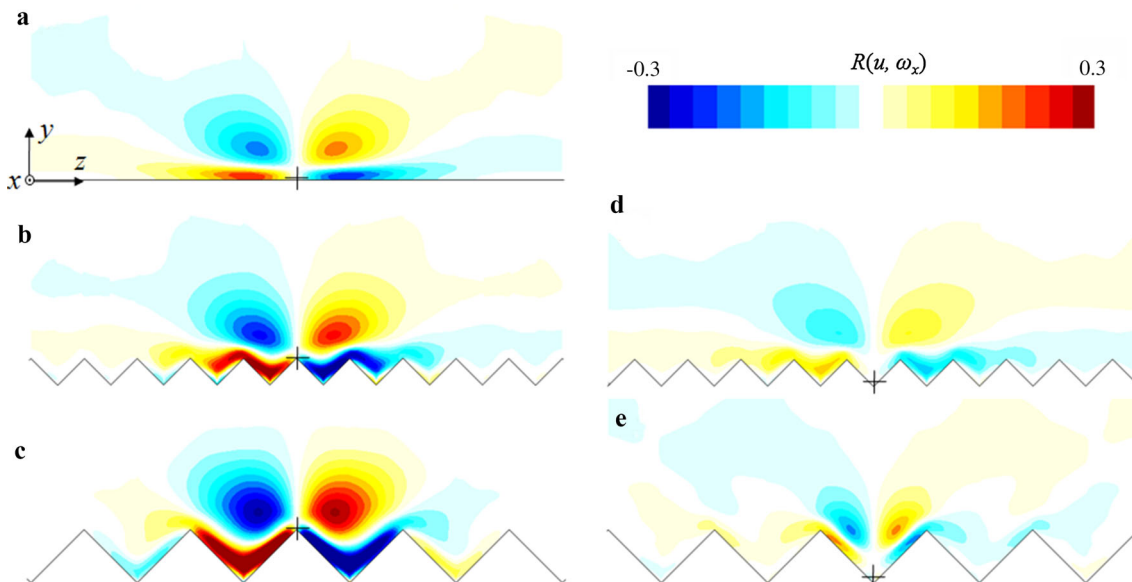

Fig. 16 Contours of $R(u, \omega_x)$ at the cross-flow plane where $x = x_r$ as y_r approaches 0. The crosses "+" mark the positions of the reference points. **a** Baseline; **b** S-20, the reference point locates above the riblet tip; **c** S-40, above tip; **d** S-20, above valley; **e** S-40, above valley

est local scales of the flow". Here we use spatial two-point correlation functions to investigate the effect of riblets on the averaged near-wall coherent structures. The two-point correlation coefficients are calculated by

$$R(\phi_A; \phi_B) = \frac{\sum \left[(\phi_A - \langle \phi_A \rangle)(\phi_B - \langle \phi_B \rangle) \right]}{(\phi_A)_{\mathrm{rms}}(\phi_B)_{\mathrm{rms}}}, \qquad (4)$$

where ϕ_A and ϕ_B represent variables at a reference point $A = (x_r, y_r, z_r)$ and at arbitrary points $B = (x, y, z)$, respectively. If ϕ_A denotes velocity u_i and ϕ_B denotes vorticity ω_j, a statistical coherent structure, the velocity–vorticity correlation structure (VVCS) [42], is exhibited using the two-point cross-correlation coefficients Ru_i, ω_j of u_i and ω_j with $i, j = 1, 2, 3$. The VVCS, which was originally proposed by Chen et al. [42], is a useful method to analyze the near-wall coherent structures. We set $x_r = 5\delta_{\mathrm{in}}$, starting from the inlet of the computation domain. As y_r varies, a family of coherent structures is exhibited. When we set y_r at the first grid point

over the riblet tip, the iso-surfaces of $R(u, \omega_x) = 0.2$ and -0.2 are displayed in Fig. 15. The streamwise velocity and vorticity are used in the calculation of the two-point correlation coefficients. Two pairs of substructures with alternate signs of correlations are evident. One pair is attached to the wall, while the other locates upper. Following the nomenclature of Chen et al. [42], we call the pair of wall-attached substructures as near-wall correlation structure (NWCS) and the pair of upper substructures as accompanying streamwise correlation structure (ASCS), both for similarity and easier comparison.

Figure 16 shows contours of $R(u, \omega_x)$ at the cross-flow plane where $x = x_r$ as y_r approaches 0. The crosses "+" mark the positions of the reference points A. For the riblet cases, y_r locate above the riblet tip (Fig. 16b, c) or above the riblet valley (Fig. 16d, e). The NWCS has a wider extent in z than in y, indicating that the vertical shear ($\partial w/\partial y$) dominates the spanwise gradient ($\partial v/\partial z$) in ω_x. Owning to the streak transient growth (STG) theory [43], it suggests

that the NWCS is attributed to the effects of the internal shear layers (or vorticity sheets) and represents an averaged motion of the near-wall vortex, in agreement with the discussion in Chen et al. [42]. In the cases with riblets the spanwise extent of the NWCS is disturbed by the inhomogeneous distribution of the wall surfaces. As y_r increases, the NWCS remains attached to the wall surfaces until it disappears for $y_r^+ > 130$, where the y_r^+ is defined by the viscous properties of the Baseline case.

The ASCS appears in upper side of the NWCS and has inclined angles to the wall, very similar to the conceptual model of the counter-rotating streamwise vortices proposed by Townsend [44]. As displayed in Fig. 16b, d, the ASCS in the drag-reducing case is lifted above the riblet tip, and a relatively small amount of riblet surface is impacted by this substructure, regardless of the spanwise location of the reference points. In the drag-increasing case, as displayed in Fig. 16c, e, the ASCS is embedded further into the riblet cove, and a larger surface area of the riblets is exposed to this substructure. As reported in Ref. [11], local regions of high skin friction on the wall are associated with the sweep motions of the streamwise vortices. The larger surface area of the riblets exposing to the ASCS in the drag-increasing case results in a larger area of local high skin frictions (drag increases) near the riblet tip. The net drag is increased in this case since the local drag increase near the riblet tip dominates over the drag reduction near the riblet valley.

This is in accordance with the observation in Fig. 10. Instantaneous visualizations of the interaction between riblets and near-wall vortical structures have been conducted in the experimental study of Lee and Lee [12] using smoke from atomized oil burned in air and in the DNS study of Choi et al. [11] using instantaneous cross-flow velocity vectors. However, sampling errors may exist in the instantaneous visualizations. In the present study, the statistical coherent structures are more quantitative to reveal the interaction between riblets and the near-wall vortical structures, which provide more insights into the drag reduction mechanism. The lift-up of the ASCS in the riblet configurations is clearly evident by examining the wall-normal distance of the cores of the ASCS to the origin of coordinate, D_y, which is shown in Fig. 17. The cores of the ASCS are determined by the maximum or minimal $R(u, \omega_x)$. Results show that the D_y in the riblet configurations has been increased in the near-wall region with $y_r/\delta_{\text{ref}} < 0.1$, and no difference is observed in the upper region with $y_r/\delta_{\text{ref}} > 0.1$.

Impeding the cross-flow motions has been hypothesized to be a key mechanism for the turbulent drag reduction with the riblets [8]. However, no direct evidence has been provided to demonstrate the riblets are capable to impede the cross-flow motions in the turbulent boundary layer. The spanwise spacing of the cores of the ASCS, D_z, are plotted in Fig. 18, as y_r varies from the nearest wall to the logarithmic region of the
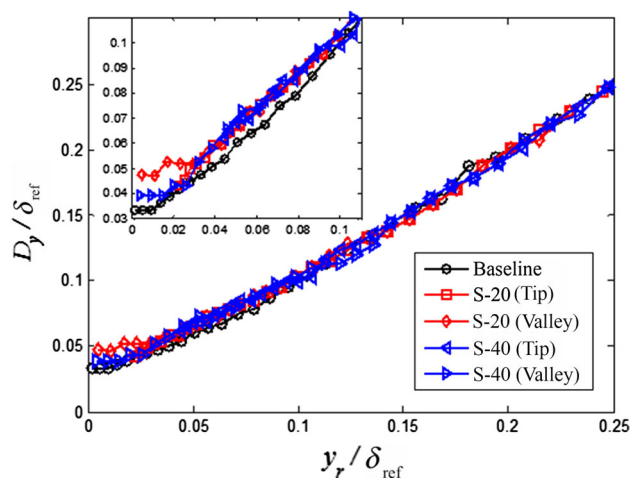

Fig. 17 Wall-normal distance of the cores of the ASCS to the origin of coordinate
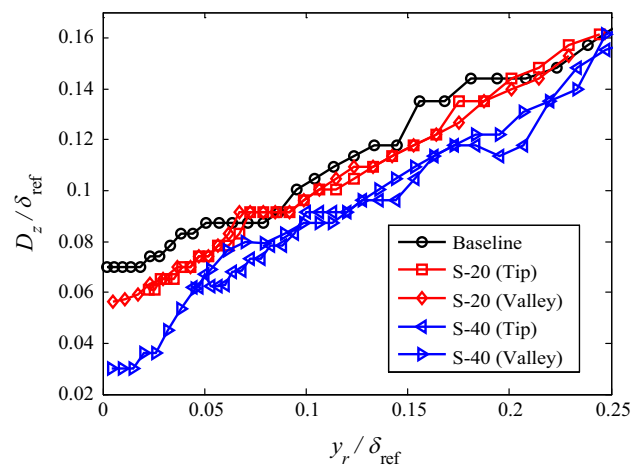

Fig. 18 Spacing of the cores of the ASCS

turbulent boundary layer. It clearly shows that with the riblets the cores of the ASCS are closer to each other than those for flow over the smooth wall, and wider riblet spacing leads to more reduction of their spanwise spacings. This feature suggests that the riblets do impede the cross-flow motions. Considering that the drag-increasing case is more effective to impede the cross-flow motions, it may suggest that impeding the cross-flow motions is not directly related with the drag reduction mechanism. Figure 19 shows spacing of the cores of the ASCS in the Baseline case, which are normalized by viscous properties. It is noteworthy that the profile of D_z^+ has a good linear fit using $D_z^+ = 0.39y_r^+ + 29.5$, slightly different with the liner fit of $D_z^+ = 0.31y_r^+ + 30.3$ by Chen et al. [42].

Two-point statistics using streamwise vorticity ω_x itself are presented here to investigate more about the near-wall coherent structures. As setting y_r approaching the wall, contours of $R(\omega_x, \omega_x)$ at the cross-flow plane where $x = x_r$
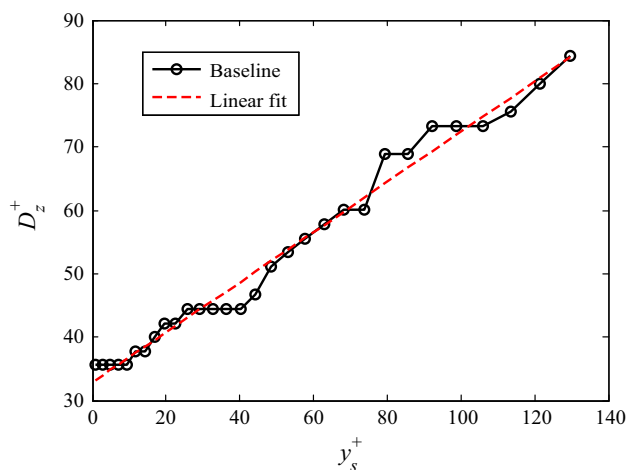
Fig. 19 Spacing of the cores of the ASCS in the Baseline case, normalized by viscous properties. The dashed line is the linear fit of the profiles

are displayed in Fig. 20. The crosses "+" mark the positions of the reference points. The two-point statistics depict a near-wall structure surrounding the reference point where $R(\omega_x, \omega_x) = 1.0$. This near-wall structure has a wider extent in z than in y, similar to the NWCS visualized by VVCS. In the riblet configurations, this near-wall structure is deflected downward when setting the reference point close to the riblet tip and tilted along the riblet wall when setting the reference point close to the riblet valley. Bulks of negative correlations are observed in the upper and lateral sides of the near-wall structure. As y_r increases, the upper negative correlations become weaker and weaker, and the lateral negative correla-

tions disappears for $y_r^+ > 7$ simultaneously accompanying with that new negative correlations appear below the positive ones. Based on these descriptions, when the reference point is set very close to the wall within $y_r^+ < 7$, the positive correlations surrounding the reference point represent the averaged organization of the low-speed streaks, and the upper negative correlations somehow reflect the averaged organization of the quasi-periodic streamwise vortices. With $y_r^+ > 7$, the positive correlations surrounding the reference point are switched to represent the averaged organization of the streamwise vortices. For instance, when setting $y_r \approx 0.07\delta_{\text{ref}}$ or $y_r^+ \approx 75$ (Baseline), contours of $R(\omega_x, \omega_x)$ at the cross-flow plane where $x = x_r$ are shown in Fig. 21. Since the reference point locates in the logarithmic region of turbulent boundary layer, the positive correlations suggest the averaged organization of the streamwise vortices. The averaged diameter of the streamwise vortices is $d^+ \approx 33$ in the Baseline case, which is in agreement with the estimation of $d^+ \approx 30$ by Kim et al. [45]. Having in mind that the riblets spacing is $s^+ = 20$ and $s^+ = 40$ respectively for the drag-reducing case and the drag-increasing case, the diameter ($d^+ \approx 33$) of the streamwise vortices is smaller than the riblet spacing for the drag-reducing case and larger than the riblet spacing for the drag-increasing case. It implies that the streamwise vortices in the drag-increasing case are able to move more freely inside the riblet coves than those in the drag-reducing case, resulting in more wetted area exposed to the sweep events of the streamwise vortices in the drag-increasing case. This feature may also be drawn from Fig. 20d, e when considering the upper negative correlations as the averaged organization of the streamwise vortices.
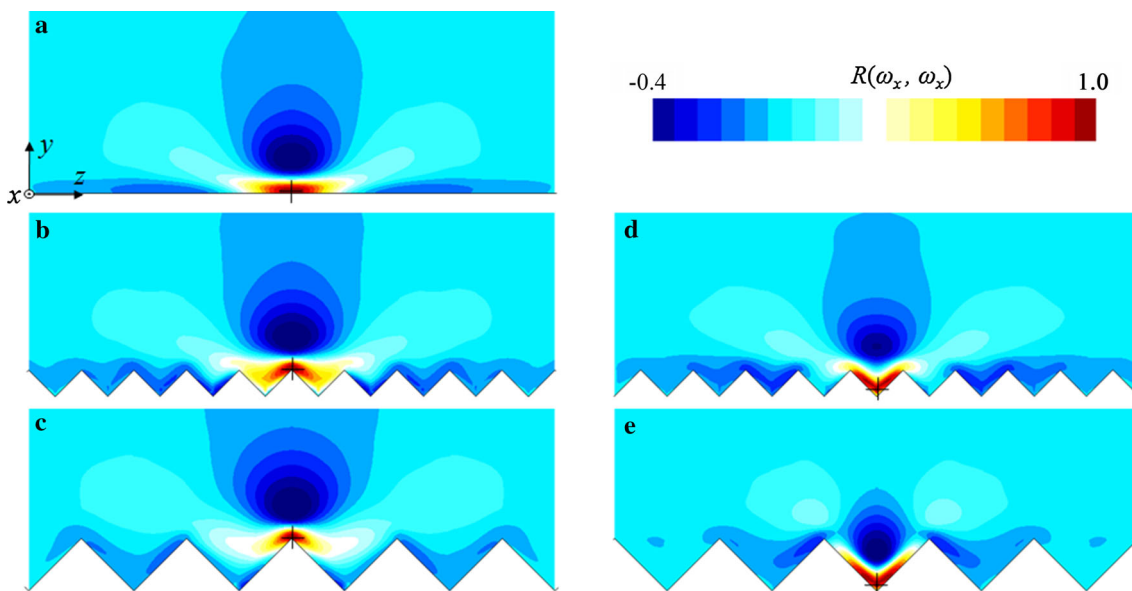

Fig. 20 Contours of $R(\omega_x, \omega_x)$ at the cross-flow plane where $x = x_r$ as y_r approaches 0. The crosses "+" mark the positions of the reference points. **a** Baseline; **b** S-20, the reference point locates above the riblet tip; **c** S-40, above tip; **d** S-20, above valley; **e** S-40, above valley

Fig. 21 Contours of $R(\omega_x, \omega_x)$ at the cross-flow plane where $x = x_r$ as $y_r \approx 0.07\delta_{ref}$. The crosses "+" mark the positions of the reference points. **a** Baseline; **b** S-20, the reference point locates above the riblet tip; **c** S-40, above tip; **d** S-20, above valley; **e** S-40, above valley
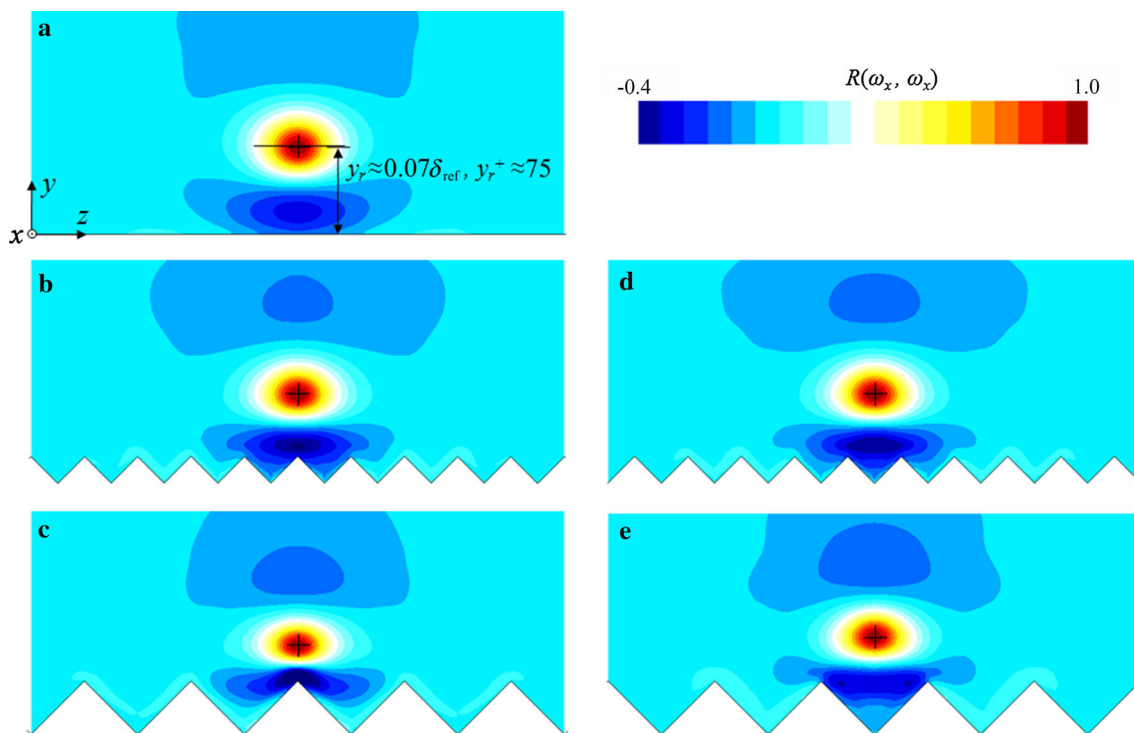

Fig. 22 Contours of $R(\omega_x, \omega_x)$ at a x–y plane where $y_r \approx 0.07\delta_{ref}$. The crosses "+" mark the positions of the reference points. **a** Baseline; **b** S-20, the reference point locates above the riblet tip; **c** S-40, above tip; **d** S-20, above valley; **e** S-40, above valley
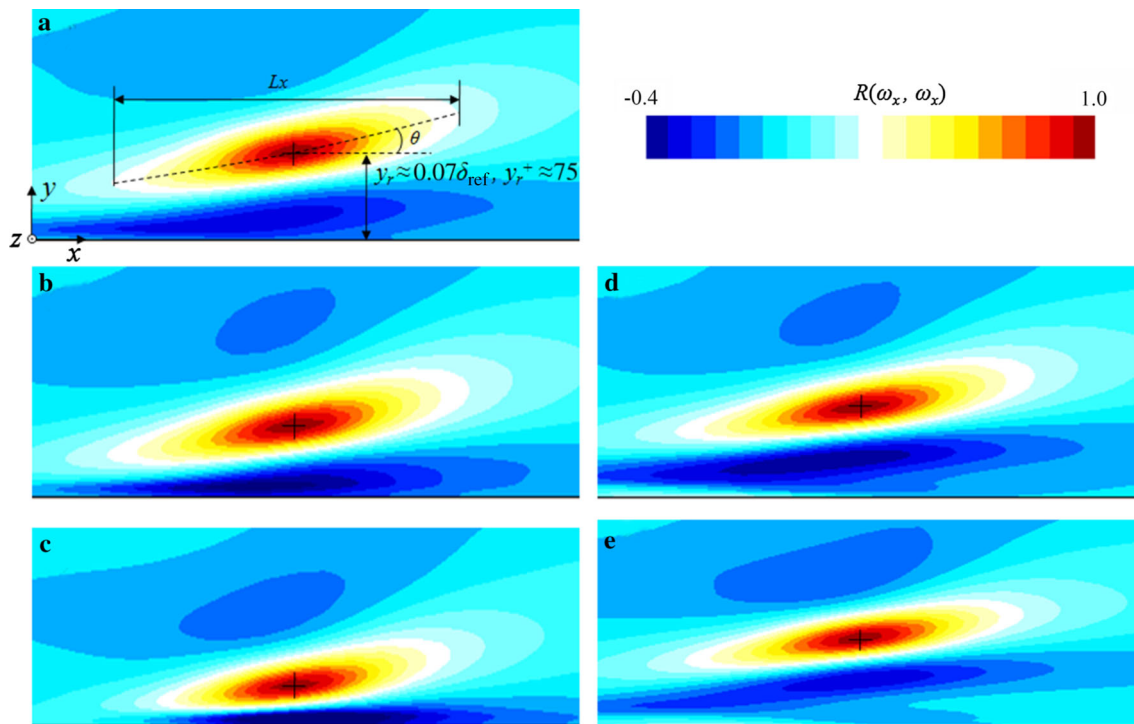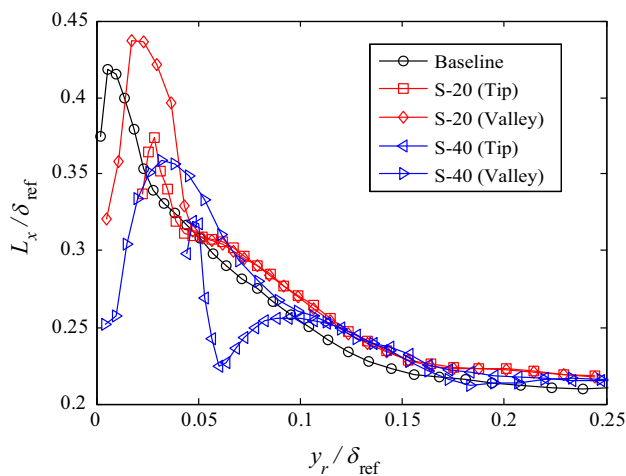
Fig. 23 Streamwise length of the averaged organization of the streamwise vortices

With $y_r \approx 0.07\delta_{ref}$ (the same as Fig. 21), a side view of the contours of $R(\omega_x, \omega_x)$ at $z = z_r$ is displayed in Fig. 22. It shows that the averaged organization of the streamwise vortices has inclined angles (θ) to the wall. The inclination angles do not change significantly in the cases with riblets. They start with 4° and approach 14° as increasing y_r. This measurement is in agreement with the observation of Rajagopalan and Antonia [46] and Chen et al. [42].

A threshold of $R(\omega_x, \omega_x) < 0.1$ is used to estimate the streamwise length of the time-averaged organization of the streamwise vortices L_x, as shown in Fig. 23. In the region very close to the wall the L_x is highly impacted by the spanwise inhomogeneity of the riblet configurations, thus no discussion is made for L_x very close to the wall. After the L_x have no apparent variation with the spanwise locations, we can find that in the cases with riblets the streamwise vortices have longer streamwise lengths.

6 Conclusions

Turbulent drag reduction with riblets has been investigated by means of DNS of a turbulent flow at $M = 0.3$ and $Re_{\delta_{in}} = 1.1 \times 10^4$ over triangular riblets with ridge angles of 45°. The spatially developing turbulent inflow is generated with a recycling and rescaling technique. Detailed validations have been conducted to assess the reliability of the DNS. A drag-reducing and a drag-increasing riblet configure are simulated with riblet spacing of $s^+ = 20$ and $s^+ = 40$, respectively. For the two riblet configures, local drag reductions are observed near riblet valley, and local drag increases are observed near riblet tip. When the drag reduction near the riblet valley dominates over the local drag increase near the riblet tip, net drag is reduced, otherwise increased.

Two-point velocity–vorticity correlation structures (VVCS) are used to examine the effects of riblets on the averaged organization of near-wall coherent structures. Two pairs of coherent structures (NWCS and ASCS) with alternate signs of correlations of $R(u, \omega_x)$ are exhibited. The NWCS is attributed to the effects of the internal shear layers (or vorticity sheets) and represents dynamics of the low-speed streaks. When there are riblets, the spanwise extent of the NWCS is disturbed by the inhomogeneous distribution of the riblet surfaces. The ASCS is similar to the conceptual model of the counter-rotating streamwise vortices proposed by Townsend [44]. The ASCS in the drag-reducing case is lifted above the riblet tip, and a relatively small amount of riblet surface is impacted by this substructure. In the drag-increasing case the ASCS is immersed further into the riblet cove, and a larger surface area of the riblets is exposed to this substructure. It provides further and quantitative evidence for the drag reduction mechanism first proposed by Choi et al. [11]. In the spanwise direction, the cores of the ASCS in the riblet configurations are shown to be closer to each other than those in flow over the smooth wall, and wider riblet spacing leads to more reduction of their spanwise distances. This feature suggests that the riblets do impede the cross-flow turbulent motions, but the change of the cross-stream motions does perhaps not explain the net drag reduction.

Two-point statistics using streamwise vorticity ω_x itself are also presented to investigate the near-wall coherent structures. The diameter of the streamwise vortices, d^+, estimated form the Baseline case, is about 33. Comparison of d^+ and the riblet spacing s^+ implies that the streamwise vortices in the drag-increasing case are enabled to move more freely inside the riblet coves than those in the drag-reducing case. Moreover, in the cases with riblets the streamwise vortices have longer streamwise lengths, but their inclination angles do not change much.

Supplementary material

Snapshots of the instantaneous streamwise vorticity and absolute vorticity from the inlet to outlet of the computational domain have been converted to movies, which are available to be downloaded from the website. The "Clean-vorticity-x.avi", "S-20-vorticity-x.avi", and "S-40-vorticity-x.avi" display contours of instantaneous streamwise vorticity for the Baseline, S-20, and S-40 case, respectively. The "Clean-vorticity-mag.avi", "S-20-vorticity-mag.avi", and "S-40-vorticity-mag.avi" display contours of instantaneous vorticity magnitude for the Baseline, S-20, and S-40 case, respectively.

References

1. Bushneil, D.M., Hefner, J.N., Viscous Drag Reduction in Boundary Layers. AIAA, 203-261 (1990)
2. Viswanath, P.: Aircraft viscous drag reduction using riblets. Progr. Aerosp. Sci. **38**, 571–600 (2002)
3. Dean, B., Bhushan, B.: Shark-skin surfaces for fluid-drag reduction in turbulent flow: a review. Philos. Trans. R. Soc. Lond. A: Math. Phys. Eng. Sci. **368**, 4775–4806 (2010)
4. Abdulbari, H.A., Mahammed, H.D., Hassan, Z.B.: Bio-inspired passive drag reduction techniques: a review. ChemBioEng Rev. **2**, 185–203 (2015)
5. Luo, Y., Xu, X., Li, D., et al.: Recent developments in fabricating drag reduction surfaces covering biological sharkskin morphology. Rev. Chem. Eng. **32**, 93–113 (2016)
6. Bacher, E.V., Smith, C.R.: Turbulent boundary-layer modification by surface riblets. AIAA J. **24**, 1382–1385 (1986)
7. Suzuki, Y., Kasagi, N.: Turbulent drag reduction mechanism above a riblet surface. AIAA J. **32**, 1781–1790 (1994)
8. Bechert, D.W., Bartenwerfer, M.: The viscous flow on surfaces with longitudinal ribs. J. Fluid Mech. **206**, 105–129 (1989)
9. Luchini, P., Manzo, F., Pozzi, A.: Resistance of a grooved surface to parallel flow and cross-flow. J. Fluid Mech. **228**, 87–109 (1991)
10. Tardu, S.F.: Coherent structures and riblets. Appl. Sci. Res. **54**, 349–385 (1995)
11. Choi, H., Moin, P., Kim, J.: Direct numerical simulation of turbulent flow over riblets. J. Fluid Mech. **255**, 503–539 (1993)
12. Lee, S.J., Lee, S.H.: Flow field analysis of a turbulent boundary layer over a riblet surface. Exp. Fluids **30**, 153–166 (2001)
13. Martin, S., Bhushan, B.: Fluid flow analysis of a shark-inspired microstructure. J. Fluid Mech. **756**, 5–29 (2014)
14. García-Mayoral, R., Jiménez, J.: Hydrodynamic stability and breakdown of the viscous regime over riblets. J. Fluid Mech. **678**, 317–347 (2011)
15. Walsh, M.J.: Riblets as a viscous drag reduction technique. AIAA J. **21**, 485–486 (1983)
16. Li, W., Nonomura, T., Fujii, K.: Mechanism of controlling supersonic cavity oscillations using upstream mass injection. Phys. Fluids **25**, 086101 (2013a)
17. Li, W., Nonomura, T., Fujii, K.: On the feedback mechanism in supersonic cavity flows. Phys. Fluids **25**, 056101 (2013b)
18. Kawai, S., Fujii, K.: Compact scheme with filtering for large-eddy simulation of transitional boundary layer. AIAA J. **46**, 690–700 (2008)
19. Nonomura, T., Fujii, K.: Overexpansion effects on characteristics of mach waves from a supersonic cold jet. AIAA J. **49**, 2282–2294 (2011)
20. Lele, S.K.: Compact finite difference schemes with spectral-like resolution. J. Comput. Phys. **103**, 16–42 (1992)
21. Visbal, M.R., Gaitonde, D.V.: On the use of higher-order finite-difference schemes on curvilinear and deforming meshes. J. Comput. Phys. **181**, 155–185 (2002)
22. Nishida, H., Nonomura, T.: ADI-SGS scheme on ideal magneto-hydrodynamics. J. Comput. Phys. **228**, 3182–3188 (2009)
23. Kawai, S.: Direct numerical simulation of transcritical turbulent boundary layers at supercritical pressures with strong real fluid effects. AIAA (2016)
24. Pirozzoli, S., Bernardini, M., Grasso, F.: Characterization of coherent vortical structures in a supersonic turbulent boundary layer. J. Fluid Mech. **613**, 205–231 (2008)
25. Sagaut, P., Garnier, E., Tromeur, E., et al.: Turbulent inflow conditions for large-eddy-simulation of compressible wall-bounded flows. AIAA J. **42**, 469–477 (2012)
26. Spalart, P.R., Allmaras, S.R.: A one equation turbulence model for aerodinamic flows. In: AIAA Paper, vol. 94 (1992)
27. Lund, T.S., Wu, X., Squires, K.D.: Generation of turbulent inflow data for spatially-developing boundary layer simulations. J. Comput. Phys. **140**, 233–258 (1998)
28. Morgan, B., Larsson, J., Kawai, S., et al.: Improving low-frequency characteristics of recycling/rescaling inflow turbulence generation. AIAA J. **49**, 582–597 (2011)
29. Sandham, N.D., Yao, Y.F., Lawal, A.A.: Large-eddy simulation of transonic turbulent flow over a bump. Int. J. Heat Fluid Flow **24**, 584–595 (2003)
30. Spalart, P.R.: Direct simulation of a turbulent boundary layer up to $Re_\theta = 1410$. J. Fluid Mech. **187**, 61–98 (1988)
31. Pirozzoli, S., Bernardini, M., Grasso, F.: Direct numerical simulation of transonic shock/boundary layer interaction under conditions of incipient separation. J. Fluid Mech. **657**, 361–393 (2010)
32. del Álamo, J.C., Jiménez, J.: Spectra of the very large anisotropic scales in turbulent channels. Phys. Fluids **15**, L41 (2003)
33. Na, Y., Moin, P.: The structure of wall-pressure fluctuations in turbulent boundary layers with adverse pressure gradient and separation. J. Fluid Mech. **377**, 347–373 (1998)
34. Walsh, M.J.: Turbulent boundary layer drag reduction using riblets. In: AIAA Paper 1982-0169 (1982)
35. Bechert, D.W., Bruse, M., Hage, W., et al.: Experiments on drag-reducing surfaces and their optimization with an adjustable geometry. J. Fluid Mech. **338**, 59–87 (1997)
36. Duan, L., Choudhari, M.M.: Effects of riblets on skin friction in high-speed turbulent boundary layers. In: AIAA Paper 2012-1108 (2012)
37. Boomsma, A., Sotiropoulos, F.: Direct numerical simulation of sharkskin denticles in turbulent channel flow. Phys. Fluids **28**, 035106 (2016)
38. Choi, H., Moin, P., Kim, J.: On the effect of riblets in fully developed laminar channel flows. Phys. Fluids Fluid Dyn. **3**, 1892–1896 (1991)
39. El-Samni, O.A., Chun, H.H., Yoon, H.S.: Drag reduction of turbulent flow over thin rectangular riblets. Int. J. Eng. Sci. **45**, 436–454 (2007)
40. Boomsma, A., Sotiropoulos, F.: Riblet drag reduction in mild adverse pressure gradients: a numerical investigation. Int. J. Heat Fluid Flow **56**, 251–260 (2015)
41. Robinson, S.K.: Coherent motions in the turbulent boundary layer. Ann. Rev. Fluid Mech. **23**, 601–639 (1991)
42. Chen, J., Hussain, F., Pei, J., et al.: Velocity-vorticity correlation structure in turbulent channel flow. J. Fluid Mech. **742**, 291–307 (2014)
43. Schoppa, W., Hussain, F.: Coherent structure generation in near-wall turbulence. J. Fluid Mech. **453**, 57–108 (2002)
44. Townsend, A.A.: Entrainment and the structure of turbulent flow. J. Fluid Mech. **41**, 13–46 (1970)
45. Kim, J., Moin, P., Moser, R.: Turbulence statistics in fully developed channel flow at low reynolds number. J. Fluid Mech. **177**, 133–166 (1987)
46. Rajagopalan, S., Antonia, R.A.: Some properties of the large structure in a fully developed turbulent duct flow. Phys. Fluids **1958–1988**(22), 614–622 (1979)